Physical properties and astrometry of radio-emitting brown dwarf TVLM513-46546 revisited

Marcin P. Gawroński,[★] Krzysztof Goździewski[★] and Krzysztof Katarzyński[★]

Centre for Astronomy, Faculty of Physics, Astronomy and Informatics, Nicolaus Copernicus University, Grudziadzka 5, PL-87-100 Toruń, Poland

ABSTRACT

We present multi-epoch astrometric observations of the M9 ultracool dwarf TVLM513-46546 that is placed at the brown dwarf boundary. The new observations have been performed with the European Very Large Baseline Interferometry Network at 6 cm band. The target has been detected at seven epochs spanning three years, with measured quiescent emission flux in the range 180–300 μJy. We identified four short-duration flaring events (0.5–2 mJy) with very high circular polarization (∼75 per cent–100 per cent). Properties of the observed radio flares support the physical model of the source that is characterized by the electron cyclotron maser instability responsible for outbursts of radio emission. Combined with Very Long Baseline Array earlier data, our detections make it possible to refine the absolute parallax $\pi = 93.27^{+0.18}_{-0.17}$ mas. Our measurements rule out TVLM513-46546 companions more massive than Jupiter in orbits with periods longer than ∼1 yr.

Key words: methods: observational – techniques: interferometric – astrometry – brown dwarfs – stars: flare – stars: individual: TVLM513-46546.

1 INTRODUCTION

Investigating properties of astrophysical objects in the Solar neighbourhood is one of the main targets of modern astrophysics regarding stellar and planetary systems statistics. Since low-mass stellar and sub-stellar population is dominant in the local volume, much effort is recently devoted to studies of M dwarfs and brown dwarfs. These objects are favourable targets to detect their low-mass companions. However, young M dwarfs are magnetically active, making it very difficult to measure their radial velocities (RV) with the precision required by contemporary planetary surveys (∼5–50 ms^{-1}), due to variable emission lines and broad molecular spectral features. Therefore ongoing RV surveys focus on M-dwarf samples that are biased towards chromospherically quiet and old objects (e.g. Rivera et al. 2005; Bailey et al. 2009; Astudillo-Defru et al. 2015; Affer et al. 2016). Fortunately, in general M-dwarfs spectral activity has much less impact on astrometric measurements.

Astrometric techniques make it possible to reach targets, which also could not be observed by transits. Indeed, the optical/infrared astrometry and direct imaging has recently revealed two sub-stellar companions orbiting a very low-mass star and a brown dwarf (Sahlmann et al. e.g. 2016, see also Sahlmann et al. 2013, 2015; Bowler et al. 2015).

The Very Large Baseline Interferometry (VLBI) technique was already successful for observations of active M dwarfs at the radio domain (e.g. Pestalozzi et al. 2000). The current performance of the global VLBI systems make it possible to measure the relative positions with sub-mas precision even of very weak radio sources (≃100 μJy) and brightness temperatures in the range of 10^6–10^7 K. It provides a unique opportunity to perform astrometric studies of magnetically active low-mass stars placed in the Solar neighbourhood. The Radio Interferometric Planet Search (RIPL) conducted with the Very Long Baseline Array[1] (VLBA) demonstrates excellent new VLBI capabilities (Bower et al. 2009, 2011).

In this work, we present new results derived in the framework of Radio-Interferometric Survey of Active Red Dwarfs (RISARD) project (Gawronski, Gozdziewski & Katarzynski 2013). Similar to RIPL, RISARD is an astrometric survey conducted with the European VLBI Network (EVN), which is dedicated for observations of very young, low-mass magnetically active M dwarfs. Our targets are placed within 10–15 pc from the Sun. Here, we focus on a nearby brown dwarf TVLM513-46546 (hereafter TVLM513; Tinney et al. 1995) placed at the distance of 10.76 ± 0.03 pc (Forbrich, Berger & Reid 2013).

The paper is structured as follows. After this introduction, we present a characterization of the target and its radio-emission in Section 2. Section 3 is devoted to our follow-up EVN astrometric observations of this object. They extend the time-window by three times to ∼7 yr between 2008 March and 2015 March and span 14 epochs, hence they double the number of high-precision astrometric positions in Forbrich et al. (2013). A formulation of our improved

★ E-mail: motylek@astro.uni.torun.pl (MPG); k.gozdziewski@umk.pl (KG); kat@astro.uni.torun.pl (KK)

[1] http://www.vlba.nrao.edu/

astrometric model and the results for all available astrometric measurements are presented in Section 4. We constrain the mass range and orbital period of a putative sub-stellar or planetary companion of TVLM513. The new observations are useful for the astrophysical characterization of the target discussed in Section 5. The paper ends with conclusions.

2 THE TVLM513 TARGET AND ITS PROPERTIES

Ultracool dwarfs (spectral class M7 and cooler, Kirkpatrick, Henry & Irwin 1997) attract a great interest as boundary objects between stars and brown dwarfs. Since the discovery of intense, non-thermal radio emission from stars at the low-mass end of the main sequence (Berger et al. 2001; Berger 2002), the ongoing radio surveys of ultracool dwarfs revealed that ~10 per cent of these objects are radio luminous (e.g. Antonova et al. 2008, 2013). Probably the most unexpected aspect of the observed radio activity from ultracool dwarfs was the detection of periodic 100 per cent circularly polarized pulses (Hallinan et al. 2007, 2008). Observations by Hallinan et al. (2007) of TVLM513 showed that electron cyclotron maser emission is responsible for these 100 per cent circularly polarized periodic pulses what implies ~kG magnetic field strengths in a large-scale stable magnetic configuration. This agrees with the measured ~kG magnetic field strengths for ultracool dwarfs via Zeeman broadening observations (Reiners & Basri 2007). Very recently, Hallinan et al. (2015) detected radio and optical auroral emissions powered by magnetospheric currents from ultracool dwarf LSR J1835+3259 what supports the hypothesis of large-scale magnetic fields present in ultracool dwarfs. Yet it is still unclear which physical mechanism (incoherent or coherent) is responsible for the quiescent component of the radio emission. The incoherent gyrosynchrotron emission was proposed as the explanation of this emission by a few authors (eg. Berger 2006; Osten et al. 2006). Recent detections of high-frequency radio emission from ultracool dwarf DENIS 1048-3956 at 18 GHz (Ravi et al. 2011) and TVLM513 at 95 GHz (Williams et al. 2015) strongly support this explanation at least in these two cases.

The observed radio luminosity of detected ultracool dwarfs shows an excess when compared with the well-known empirical Güdel–Benz relation between radio and X-ray luminosity, L_{radio} and L_X, respectively, which reads as $L_{\mathrm{radio}}/L_X \sim 5$ for magnetically active stars (Güdel & Benz 1993). The theoretical model explaining the Güdel–Benz relation assumes chromospheric evaporation (Allred et al. 2006). In this scenario, the X-ray emission results from the heating and evaporation of chromospheric plasma caused by non-thermal beamed electrons, which produce gyrosynchrotron radio emission (Neupert 1968). All ultracool dwarfs detected in the radio bands contravene the Güdel–Benz relation by orders of magnitude. This suggests that the chromospheric evaporation model is not valid for these objects.

TVLM513-46546 is an M9 ultracool dwarf placed just at the brown dwarf boundary (Hallinan et al. 2006). Due to its wide activity spanning from the radio domain to the X-rays, TVLM513 is one of the most intensively studied ultracool dwarfs. The Baraffe models (Baraffe et al. 2003) estimate the mass of TVLM513 in the range 0.06–0.08 $M_\odot$, and its radius $\simeq 0.1$ $R_\odot$ for ages older than 0.5 Gyr. Wolszczan & Route (2014) estimated the rotation period $\simeq 1.96$ h using techniques similar to pulsar timing. TVLM513 exhibits a variable Hα emission and a lack of Li at 670.8 nm (Reid et al. 2002). The Hα emission changes moderately with time, indicating some chromospheric activity. The observed radio emission suggests a

Table 1. The observational log of our astrometric survey of TVLM513.

Project code	Date (day)	(UTC)	Epoch (JD-2450000)	Conv beam (mas)	(°)
EG053a	2011 Mar 11	04:07–05:29	5631.7001	9.4 × 7.4	−70
EG053b	2011 Mar 12	03:53–05:14	5632.6899	10.2 × 9.2	26
EG065D	2012 Oct 9	13:11–14:20	6210.0705	8.7 × 5.7	−59
EG065E	2012 Nov 14	07:51–09:25	6245.8597	9.6 × 5.3	−41
EG082A	2013 Dec 4	05:29–07:37	6630.7729	9.2 × 4.9	−46
EG082D	2014 Jun 24	21:28–23:42	6823.4410	11.7 × 5.2	50
EG082E	2015 Mar 25	06:05–08:28	7106.8031	15.8 × 4.6	64

multipolar magnetic field, with the strength as high as 3 kG (Hallinan et al. 2006). TVLM513 is also the first ultracool dwarf detected with the use of VLBI technique. Forbrich & Berger (2009) observed this object with the VLBA at 8.5 GHz using the inner seven stations. They recorded unresolved emission from TVLM513. With the higher spatial resolution allowed by the whole VLBA network, the source appears marginally resolved with a low signal-to-noise ratio.

Forbrich & Berger (2009) concluded that TVLM513 could be a binary system with the projected separation of ~1 mas. Motivated by first VLBI observations of TVLM513, Forbrich et al. (2013) performed an astrometric survey for a sub-stellar companion using long-term VLBA observations in 2010 and 2011. The survey consisted of eight epochs and radio images of TVLM513 were detected six times. Based on these observations, Forbrich et al. (2013) excluded companions more massive than 3.8 M_{Jup} at 16-d orbit and 0.3 M_{Jup} with the orbital period of 710 d, respectively. The existence of a putative companion to TVLM513 is yet uncertain. Recently, Leto et al. (2016) attributed the observed periodic radio flares in TVLM513 (Hallinan et al. 2006) to the auroral emission, analogous to the system of Jupiter and Io. In their model, the ~2 h cyclic pulses may be explained by the presence of a planet orbiting within the TVLM513 magnetosphere at short (<24 h) orbital periods, roughly within 5-15 radii of the object. This hypothesis reinforces the motivation for further, systematic radio- and high-precision astrometric monitoring of TVLM513.

3 NEW EVN OBSERVATIONS AND DATA REDUCTION

We made standard continuum observations of TVLM513 centred at 4.99 GHz during seven observational epochs. Stations from Effelsberg, Jodrell Bank (MkII), Medicina, Noto, Onsala, Toruń and Westerbork (phased array) participated in our observations (observation codes EG053, EG065D, EG065E, EG082A, EG082D and EG082E, see Table 1 for details). We used the EVN in e-VLBI mode of observations using the phase-referencing technique. The data were recorded at 1 Gb s^{-1} rate, providing the total bandwidth of 128 MHz divided into eight base-band channels with the bandwidth of 16 MHz each. The first epoch was separated for two parts due to limited time allocation and both segments were considered during the reduction as separated epochs. Switching cycle of 5 min was used (3.5 min for target and 1.5 min for phase calibrator J1455+2131). We also observed secondary calibrator J1504+2218 applying the same switching cycle. J1504+2218 is a flat-spectrum compact source located near TVLM513, which was selected from the Cosmic Lens All-Sky Survey.[2] TVLM513 and J1455+2131 are separated by 1°8, TVLM513 and J1504+2218

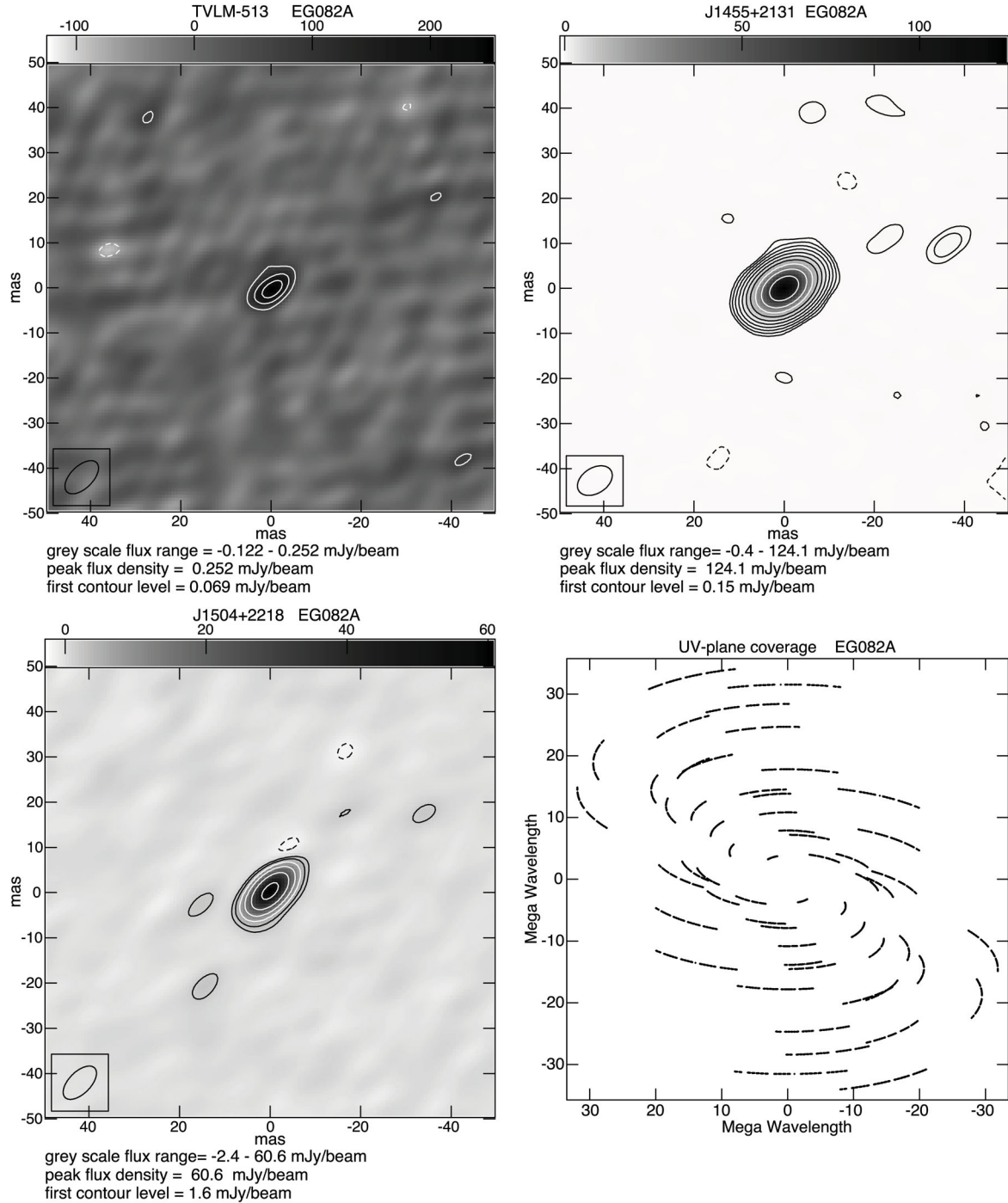[2] www.jb.man.ac.uk/research/gravlens/class/class.html

TVLM-513 EG082A
grey scale flux range = -0.122 - 0.252 mJy/beam
peak flux density = 0.252 mJy/beam
first contour level = 0.069 mJy/beam

J1455+2131 EG082A
grey scale flux range= -0.4 - 124.1 mJy/beam
peak flux density = 124.1 mJy/beam
first contour level = 0.15 mJy/beam

J1504+2218 EG082A
grey scale flux range= -2.4 - 60.6 mJy/beam
peak flux density = 60.6 mJy/beam
first contour level = 1.6 mJy/beam

UV-plane coverage   EG082A

Figure 1. Examples of detections in our observational campaign. Top left panel: TVLM513, top right panel: J1455+2131, bottom left panel: J1504+2218. All presented radio maps are based on the data derived during epoch EG082A. The first contour corresponds to the detection limit of $\simeq 3\sigma$. Subsequent contour levels are multiplied by a factor of 2. The insets show the size of the restoring beam. Bottom right panel: a typical TVLM513 observation *uv*-plane coverage (also for EG082A).

by $0\overset{s}{.}9$, J1455+2131 and J1504+2218 by $2\overset{\circ}{.}2$, respectively. During sessions EG053, EG065D and EG065E, two switching cycles for J1504+2218 observations were added: before and after observations of TVLM513. In the case of EG082, one J1504+2218 switching cycle was added at the beginning of observations and then it was repeated every five TVLM513 switching cycles. This approach resulted in comparable integration time for J1504+2218 during all experiments but better *uv*-plane coverage. J1504+2218 was observed

to examine the phase-referencing success. We also measured the position of J1504+2218 at each epoch of scheduled observations.

The data reduction process was carried out using the standard NRAO AIPS[3] procedures. The visibility data were inspected for quality, and noisy points were removed using AIPS task EDITR. Maps of

[3] www.aips.nrao.edu/index.shtml

Table 2. Astrometric position measurements and radio fluxes of TVLM513 and J1504+2218 collected during the survey. Astrometric uncertainties are formal errors of the AIPS best-fitting target's positions and do not include any systematic effects.

Project code	α (J2000)	$\Delta \alpha$ (mas)	δ (J2000)	$\Delta \delta$ (mas)	TVLM513 $S_{5\,GHz}$ (μJy)	J1504+2218 $S_{5\,GHz}$ (mJy)
			TVLM513 position			
EG053a	15 01 08.157 048	0.63	22 50 01.427 52	0.45	238 ± 51	66.5 ± 1.3
EG053b	15 01 08.157 015	0.35	22 50 01.429 50	0.40	318 ± 47	–
EG065D	15 01 08.143 333	0.23	22 50 01.267 89	0.18	331 ± 41	41.5 ± 1.4
EG065E	15 01 08.146 844	0.32	22 50 01.241 79	0.32	360 ± 45	52.2 ± 1.3
EG082A	15 01 08.145 671	0.30	22 50 01.170 79	0.27	269 ± 41	61.3 ± 0.8
EG082D	15 01 08.136 623	0.47	22 50 01.253 55	0.40	227 ± 42	58.4 ± 0.7
EG082E	15 01 08.143 284	0.57	22 50 01.176 45	0.35	226 ± 37	41.8 ± 0.8
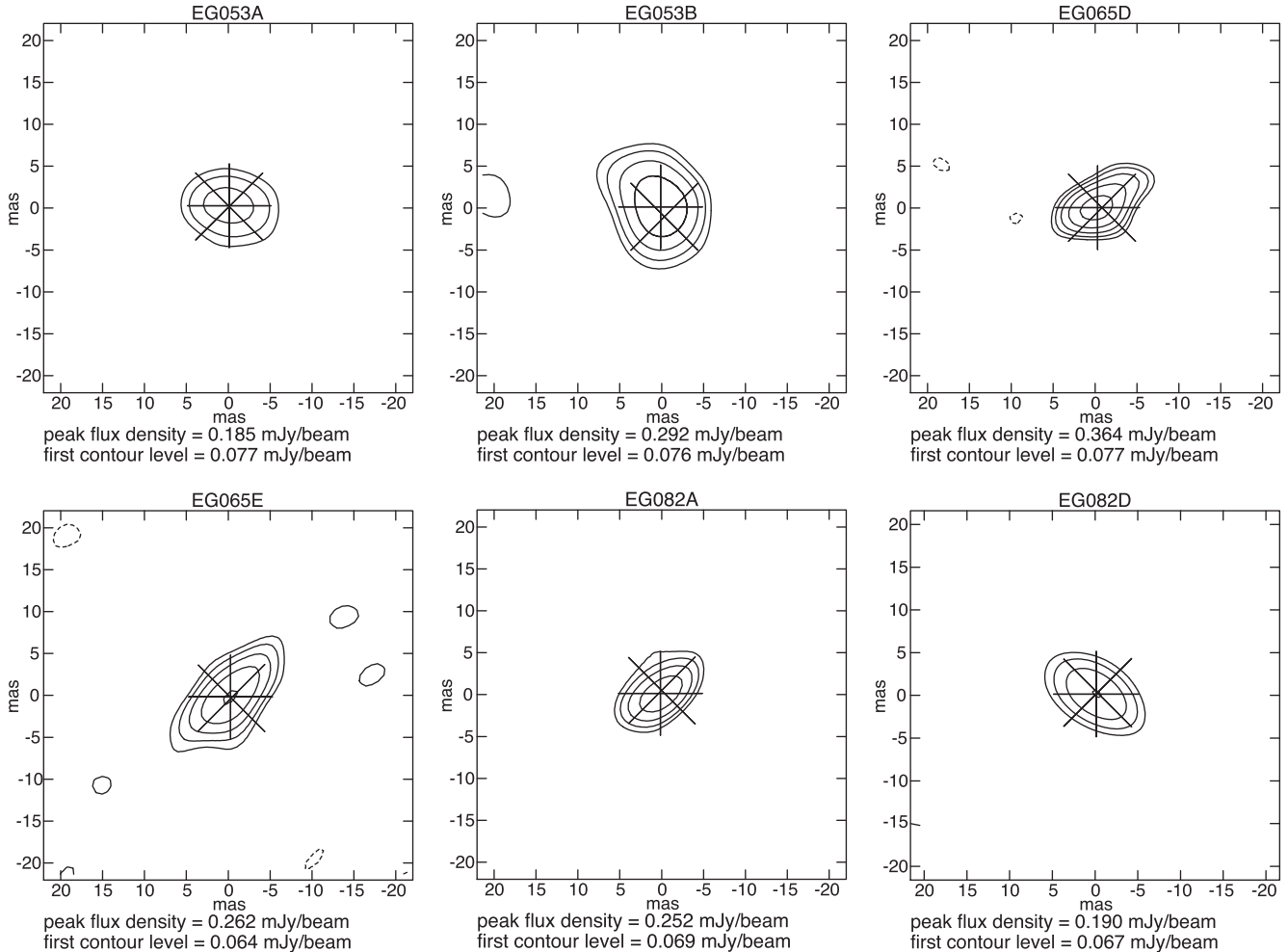
Figure 2. Radio maps of TVLM513 based on data collected during RISARD project. The first contour corresponds to the detection limit of $\simeq 3\sigma$. Successive contour levels are multiplied by a factor of 2. The + symbols mark the measured positions, and the × symbols represent the model astrometric position at the particular epoch of observations, respectively.

the phase calibrator J1455+2131 were created separately for each epoch and were used as a reference model for the final fringe-fitting. Before the fringe-fitting, we corrected ionospheric Faraday rotation and dispersive delay using AIPS task TECOR. The IMAGR task was used to produce the final total intensity images of all our sources. Examples of detections during epoch EG082A are illustrated as radio maps in Fig. 1. Radio fluxes and estimated positions of TVLM513 and J1504+2218 were then measured by fitting Gaussian models, using AIPS task JMFIT and are presented in Table 2 and illustrated in Figs 2 and 3. In order to study the radio-emission variability of

TVLM513, we reconstructed its light curves using AIPS task DFTPL. Before the application of DFTPL, we searched for background objects within 3×3 arcsec^2 around TVLM513 position and none were found. If a background object would be detected then the resulting source model should be subtracted from the visibility data. Its side lobes and shape changes of the synthesized beam could result in flux variations over the radio map and they might 'contaminate' the real variability or even may generate a false signal.

Understanding sources of uncertainties of astrometric VLBI observations is crucial for their correct estimation. There are a few
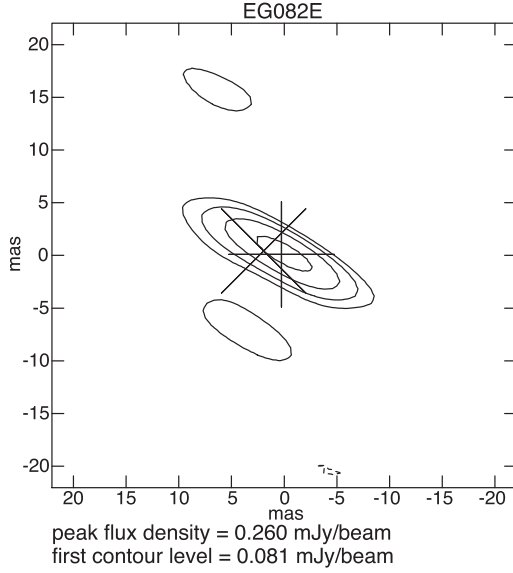
Figure 3. Radio maps of TVLM513 based on the observational data collected during RISARD project. The first contour corresponds to the detection limit of $\simeq 3\sigma$. Successive contour levels are multiplied by a factor of 2. The + symbol marks the measured position and the × symbol represents the model position at the epoch of observations, respectively.

origins of systematic errors, like the residual phase in phase-referencing, sub-mas changes of the phase calibrator structures or differences between optical path lengths for the target and the phase calibrator. The latter are caused by the atmospheric zenith delay residuals. There are mainly two different solutions of this problem. Assuming uncorrelated and normal uncertainties, one may introduce a priori introduced 'error floor' added in quadrature to raw uncertainties in order to obtain the reduced $\chi_\nu^2 \simeq 1$ (e.g. Forbrich et al. 2013; Chibueze et al. 2014). Additional interferometric observations of compact extragalactic sources spread over the sky are used to measure broad-band delays (Reid et al. 2009). It should be also mentioned that properties of M-dwarf radio emission could result in further scatter of astrometric measurements. Benz, Conway & Gudel (1998) showed that the radio corona of an active M-dwarf UV Cet B varies in size and position during a large radio flare. However, the impact of flaring events on the radio astrometry could be reduced if it is possible to remove such events from the analysis and the quiescent emission is strong enough to obtain radio images with reasonable SNR $\gtrsim 5$. We detected strong ~ 1 mJy, circularly polarized flares, which occurred during our observations (see Section 5 for details). These events spanned short time intervals ($t \lesssim 3$ min) in comparison with the duration of observations (~ 2 h of integration time per epoch). Therefore we decided to not remove the identified flares from the mapping process.

Here we present a different, systematic statistical approach to the proper optimization of astrometric model, equations (1)–(2), in the presence of unspecified error factors. It is based on the maximal likelihood function and Markov chain Monte Carlo (MCMC) exploration of the parameters space. The error floor estimated in this way accounts for different systematic effects, spanning atmospheric phase effects, a possible binarity of the target, and the motion of unseen, low-mass companions.

4 ASTROMETRIC MODEL AND ITS OPTIMIZATION

To determine the parallax and components of the proper motion, we apply a general, seven-element astrometric model with the secular acceleration terms:

$$\alpha(t_i) = \alpha_0 + \mu_\alpha(t_i - t_0) + \pi_\alpha(t_i, \alpha, \delta) + a_\alpha(t_i - t_0)^2, \quad (1)$$

$$\delta(t_i) = \delta_0 + \mu_\delta(t_i - t_0) + \pi_\delta(t_i, \alpha, \delta) + a_\delta(t_i - t_0)^2, \quad (2)$$

where (α_0, δ_0) are the target's ICRF coordinates and (μ_α, μ_δ) are components of the proper motion at the initial epoch t_0, respectively; (π_α, π_δ) are the parallax factors (i.e. the parallax π projected on to the coordinates axes), and (a_α, a_δ) are components of the secular acceleration relative to the initial epoch t_0. The secular acceleration terms are included to express a possible long-term perturbation to the inertial motion of the target and/or the perspective (geometric) acceleration. We considered also five-elements model without the acceleration terms. (It will be explained below that in fact our five- or seven-parameter models are optimized with an additional parameter scaling measurements errors.)

To get rid of (α, μ_δ) and (δ, μ_δ) correlations, we choose the initial epoch t_0 as the mean of all observational epochs t_i weighted by uncertainties σ_i ($i = 1, \dots, N$):

$$t_0 = \frac{\sum_i^N t_i w_i}{\sum_i^N w_i}, \quad w_i = \frac{1}{\sigma_i}. \quad (3)$$

Since our preliminary fits revealed $\chi_\nu^2 \sim 2$ suggestive for underestimated uncertainties, we optimized the maximum likelihood function $\mathcal{L}$:

$$\log \mathcal{L} = -\frac{1}{2} \sum_{j,t} \frac{(\text{O-C})_j^2}{\sigma_j^2} - \frac{1}{2} \sum_j \log \sigma_j^2 - \frac{1}{2} M \log 2\pi, \quad (4)$$

where $(\text{O-C})_{j,t}$ is the (O-C) deviation of the observed $\alpha(t_i)$ or $\delta(t_i)$ at epoch t_i from its astrometric ephemeris, and their uncertainties are $\sigma_j^2 \to \sigma_j^2 + \sigma_f^2$ with a parameter σ_f scaling raw uncertainties (the error floor), and $j = 1 \dots, M$ where $M = 2N$ is the total number of (α, δ) measurements. We assume that uncertainties σ_j are Gaussian and independent. By introducing the scaling of uncertainties, we aim to determine the error floor in a self-consistent manner, instead of fixing it a posteriori, as in Forbrich et al. (2013).

Combined seven VLBA measurements in Forbrich & Berger (2009) and Forbrich et al. (2013) with our seven EVN detections result in 28 (α, δ) datums, spanning $\Delta t = 2550.9222$ d. Given raw uncertainties in this data set, we computed the initial epoch t_0 = JD 2455 424.197 63 in accord with equation (3).

We optimized the log $\mathcal{L}$ function indirectly with the MCMC technique. We determine the posterior probability distribution $\mathcal{P}(\boldsymbol{\xi}|\mathcal{D})$ of astrometric model parameters $\boldsymbol{\xi} \equiv [\alpha_0, \delta_0, \pi, \mu_\alpha, \mu_\delta, a_\alpha, a_\delta, \sigma_f]$ in equations (1)–(2), given the data set $\mathcal{D}$ of all astrometric observations (understood as α_i and δ_i components): $\mathcal{P}(\boldsymbol{\xi}|\mathcal{D}) \propto \mathcal{P}(\boldsymbol{\xi}) \mathcal{P}(\mathcal{D}|\boldsymbol{\xi})$, where $\mathcal{P}(\boldsymbol{\xi})$ is the prior, and the sampling data distribution $\mathcal{P}(\mathcal{D}|\boldsymbol{\xi}) \equiv \log \mathcal{L}(\boldsymbol{\xi}, \mathcal{D})$. For all parameters, besides the acceleration terms, we define priors as flat (or uniform improper) by placing limits on model parameters, i.e. $\alpha_0 > 0$, $\delta_0 > 0$, $\mu_\alpha > 0$, $\mu_\delta > 0$ $\pi > 0$ and $\sigma_f > 0$. For the acceleration terms, whose magnitude is unspecified, we applied the Jeffreys prior:

$$\mathcal{P}(\xi) = \frac{1}{\xi_{\min} + \xi},$$

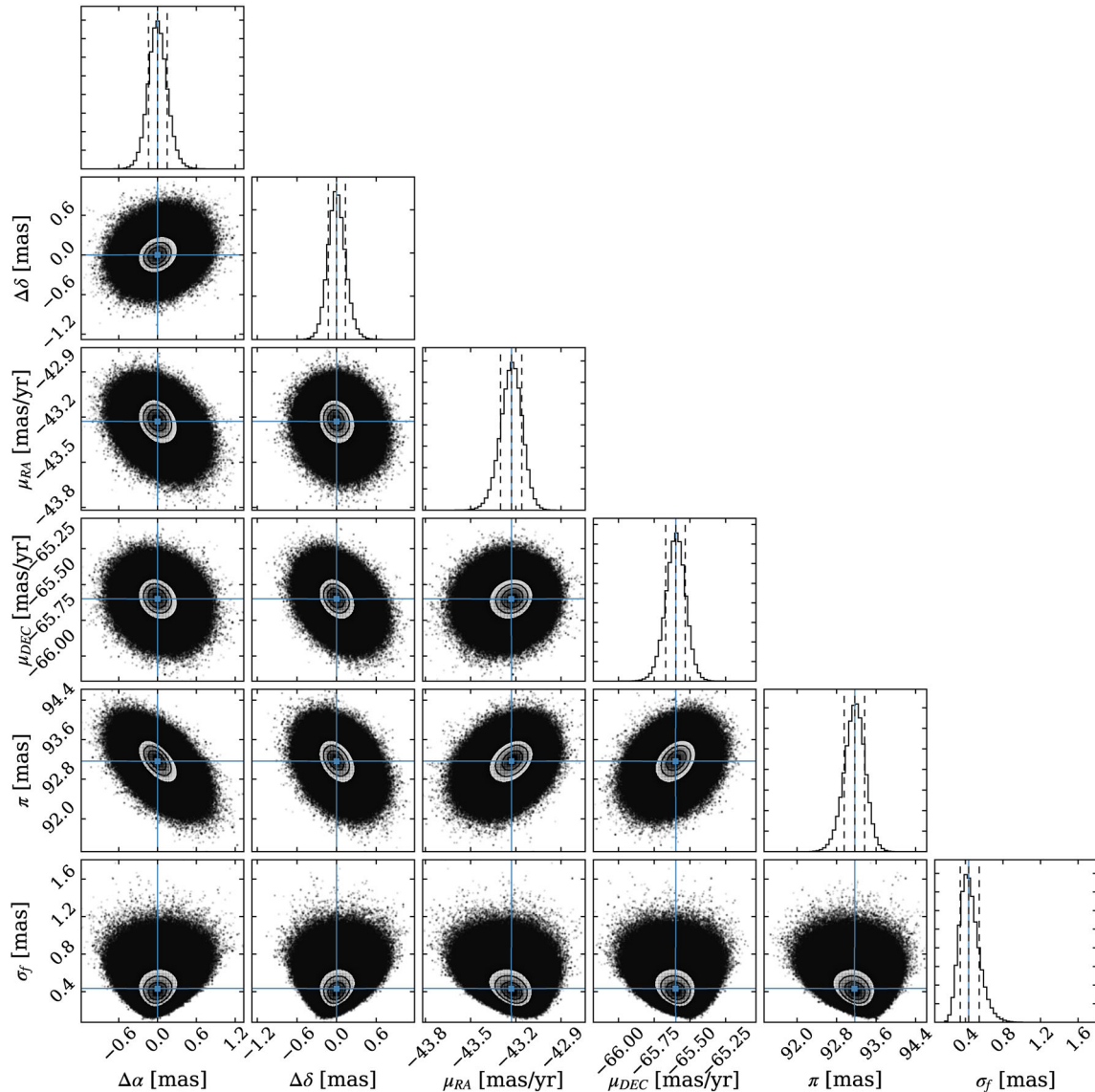where $\xi_{\min}$ is a small value to avoid underflows.

Figure 4. One- and two-dimensional projections of the posterior probability distribution for all free parameters of the astrometric five-elements model. The MCMC chain length is 256 000 iterations in each of 640 different initial conditions in a small ball around a preliminary astrometric model derived with a common function minimization. Contours indicate 16th, 50th and 84th percentiles of the samples in the posterior distributions. Crossed lines illustrate the best-fitting parameters displayed in Table 3.

To perform the MCMC sampling of the posterior, we used the affine-invariant ensemble MCMC sampler (Goodman & Weare 2010) encoded in a great EMCEE package invented and developed by Foreman-Mackey et al. (2013). To compute the parallax factors, we used the DE405 ephemeris and subroutines from the NOVAS package (Kaplan et al. 2012).

We performed a number of experiments by increasing the MCMC chain lengths up to 512 000 samples. The posterior probability distribution for the five-elements model is illustrated in Fig. 4. It shows one- and two-dimensional projections of the posterior for all free parameters of the model. A well-defined solution is apparent. No significant parameter correlations are present. The best-fitting parameter values and their uncertainties estimated between the 16th and 86th percentile are displayed in Table 3 and the on-sky motion of the target is illustrated in Fig. 5. The residuals to the five-parameter model are illustrated in Fig. 6. The best-fitting solution exhibits the

Table 3. Parameters of the best-fitting solution at the middle-arc epoch $t_0 = \text{JD } 2455\,424.197\,63$.

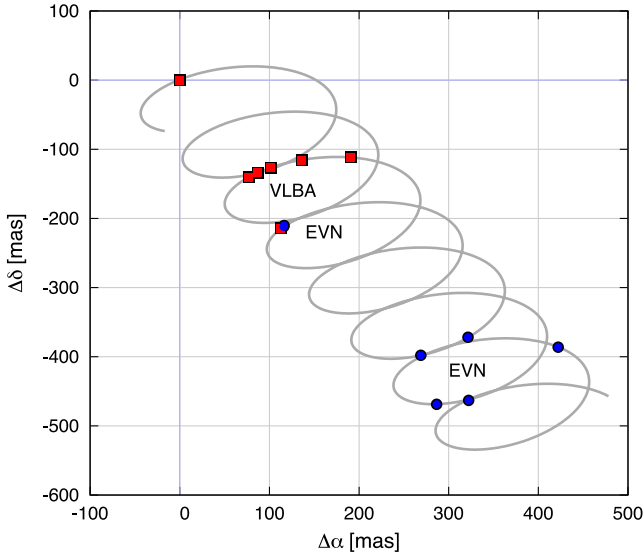| Parameter	Five-element fit	Seven-element fit
α_0	$15^{\text{h}}01^{\text{m}}8\overset{\text{s}}{.}152\,19^{+0.00009}_{-0.00010}$	$15^{\text{h}}01^{\text{m}}8\overset{\text{s}}{.}15219^{+0.00009}_{-0.00010}$
δ_0	$22°50'1\overset{''}{.}424\,70^{+0.00075}_{-0.00070}$	$22°50'1\overset{''}{.}42470^{+0.00013}_{-0.00014}$
μ_α (mas yr^{-1})	$-43.23^{+0.08}_{-0.07}$	$-43.13^{+0.08}_{-0.07}$
μ_δ (mas yr^{-1})	$-65.60^{+0.08}_{-0.07}$	$-65.50^{+0.07}_{-0.07}$
a_α (mas cyr^{-2})	–	$-12.5^{+5.1}_{-4.8}$
a_δ (mas cyr^{-2})	–	$-11.3^{+4.5}_{-4.5}$
parallax π (mas)	$93.17^{+0.21}_{-0.20}$	$93.27^{+0.18}_{-0.17}$
σ_f (mas)	$0.43^{+0.10}_{-0.12}$	$0.36^{+0.08}_{-0.10}$

Figure 5. Sky-projected, five-parameter astrocentric model of TVLM513 positions (grey curve) overplotted with the VLBA (red filled rectangles) and with all new EVN detections (blue filled circles, this work), relative to the first observation in (Forbrich et al. 2013).

error floor as large as 0.43 mas, which is roughly two times larger than estimated by Forbrich et al. (2013) for their VLBA observations alone.

Given the astrometric residuals to the five-parameter model, we may estimate the mass range of a hypothetical companion, which could be present below the detection limit. Assuming that such a companion exists in a circular Keplerian orbit with semimajor axis a, orbital period P_p and mass m_p, such a body would cause the reflex motion of the target around the barycentre with an angular semi-amplitude of

$$\Theta = \frac{m_p}{m_\star} \left[\frac{P_p^2}{4\pi^2} k^2 (m_p + m_\star) \right]^{-1/3}, \quad (5)$$
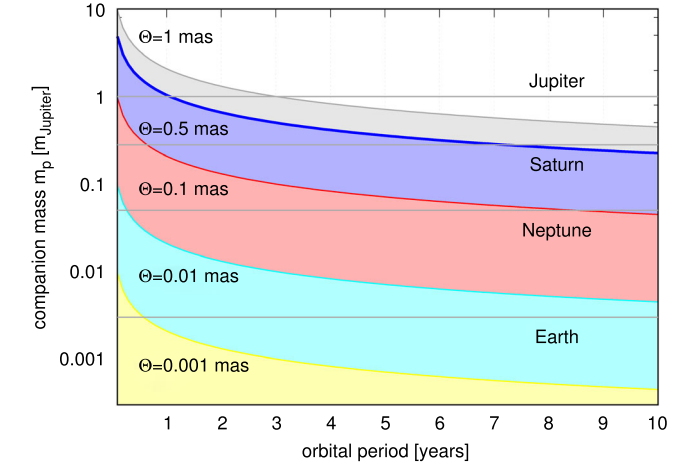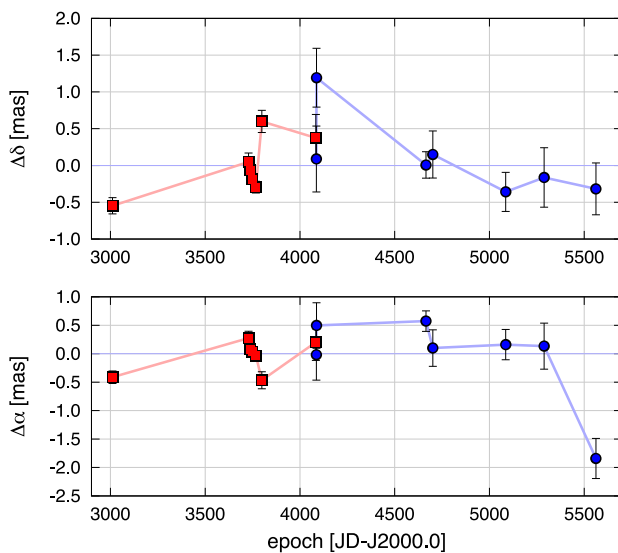
Figure 7. Astrometric detection limits for a companion to TVLM513 in the (orbital period, mass) space (see equation 5) for the mass of TVLM513 $m_\star = 0.08\,M_\odot$ and its derived distance $d = 10.733$ pc.

where $m_\star$ and m_p are the masses of the star and its companion, respectively, k^2 is the Gauss gravitational constant and P_p is the orbital period of the companion, see also Forbrich et al. (2013). For a known or assumed mass of the binary and given its orbital period and angular separation Θ from the primary, this relation may be solved w.r.t. m_p. Parametric plots $m_p \equiv m_p(P_p, \Theta)$ for a few borderline angular separations are shown in Fig. 7. Corresponding mass detection levels for a few characteristic objects are labelled.

Unfortunately, the sampling and relatively low astrometric accuracy of our EVN measurements does not make it possible to resolve any clear, systematic reflex motion of the primary (the right-hand panel of Fig. 6).

Moreover, astrometric positions at two epochs of EG053b and EG082E (Fig. 3) deviate by $\gtrsim 1$–2 mas from the five-parameter model. These excessively large discrepancies could be most likely explained through pure observational and local effects. During EG053b (2011 March 12) a strong geomagnetic storm was present
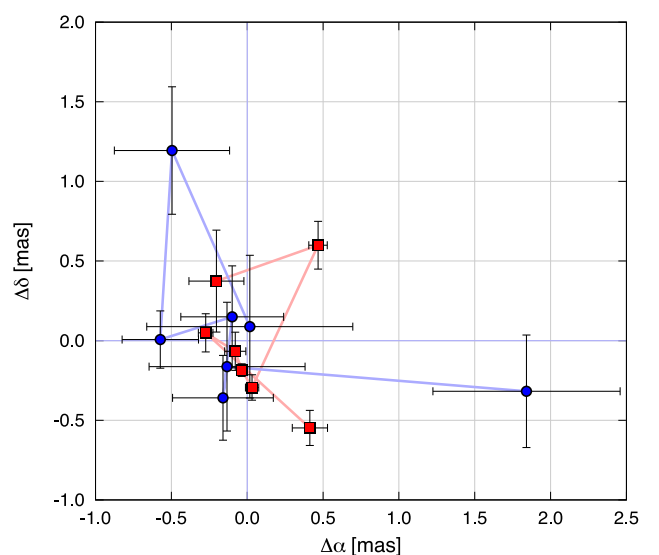

Figure 6. Residuals in right ascension (α) and declination (δ) to five-parameter astrocentric model (equations 1–2 and Fig. 5) plotted as a function of the observational epochs (the left-hand column). A plot in the right-hand panel shows the residuals in the coordinates plane. Error bars mark the reported, instrumental uncertainties that do not include systematic effects. The VLBA measurements are marked with red filled rectangles and the EVN data (this paper) are marked with blue filled circles.
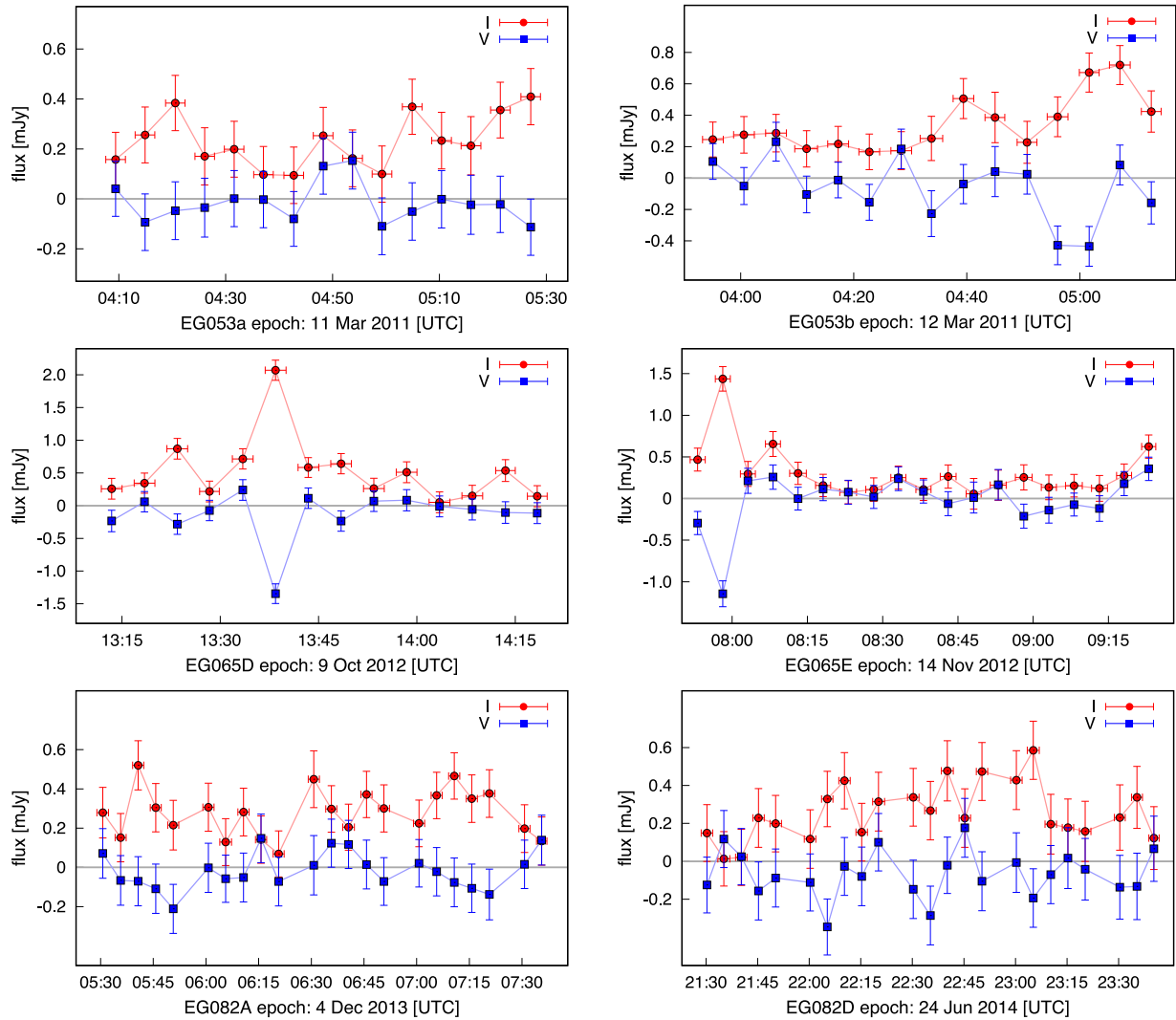
Figure 8. Observed TVLM513 light curves based on observations from RISARD project. The total intensity (Stokes *I*, red filled circles) and circularly polarized (Stokes *V*, blue filled rectangles) radio flux at 4.99 GHz is presented. Flares of right circularly polarized emission (positive *V* values) and left circularly polarized emission (negative *V* values) are detected. The error bars represent 1σ error for flux and the length of individual integrations during the phase-referencing observations for time (identical for *I* and *V* measurements). Right circular polarization is represented by positive *V* values and left circular polarization is represented by negative *V* values. Lines connecting the measurement points are shown merely to guide the viewer's eye.

in the Earth ionosphere and the aurora was visible all above Europe. At the EG082E epoch, TVLM513 elevation for the European station was low ($20°–30°$ above the horizon) and sparse *uv*-coverage resulted in a large, elongated convolution beam. These conditions of observations lead to extensive phase errors that result in shifted and non-Gaussian radio images of the star. That is especially important in the case of elongated convolution beams.

Yet we attempted to model a potential curvature effect with seven-parameter model, equations (1) and (2). The results are shown in the right-hand column of Table 3. At this time, the error floor is slightly smaller than for the five-parameter model, and the curvature coefficients are roughly -12 mas cy^{-2}. Such large values might indicate a massive companion and/or a significant perspective acceleration. However, given the apparent curvature is caused by two strongly outlying measurements (Fig. 6), we found that the residuals actually vary within ~ 0.5 mas, when centred at the t_0 epoch position. Therefore we may rule-out companions more massive than Saturn in $\gtrsim 7$-yr orbit or Jupiter in $\gtrsim 1$-yr orbit. However, very short period companions (roughly below ~ 1 yr time-scale) within mass

limits illustrated in Fig. 7 cannot be excluded due to sparse sampling. Our estimates are consistent with the results of Forbrich et al. (2013). Unfortunately, we cannot confirm nor rule their hypothesis of short-period companion in ~ 16 d orbit, as well as a putative close-in, short-period planet triggering periodic auroral activity due to the interaction with the magnetosphere of TVLM513 (Leto et al. 2016). We note that such an explanation of the observed periodic radio pulses from low-mass stars has been originally proposed by Hallinan et al. (2015). Regrettably, the astrometric observations in Forbrich et al. (2013) and in this work are currently not enough sensitive to detect such short-period planets.

5 PROPERTIES OF OBSERVED RADIO EMISSION

Since we observed TVLM513 across a wide time window of four years (between 2011 March to 2015 March), the EVN data make it possible to track the radio variability for over short (a few minutes) to long (a few months) time-scales. The radio emission traces particle
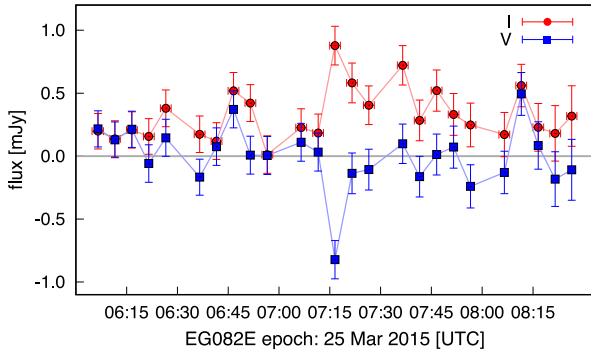
Figure 9. TVLM513 light curves continued, see Fig. 8.

acceleration by magnetic field in stellar coronae, and corresponds to incoherent (gyrosynchrotron emission) or coherent radiations (electron cyclotron maser or plasma emission).

Previous observations showed that the observed TVLM513 radio emission consists of two components, the persistent emission and bursts of highly circularly polarized radiation (e.g. Hallinan et al. 2007). In order to trace the highly variable component, we calculated averaged values of Stokes parameters I and V for each individual scan over the TVLM513 source during phase-referencing observations (3.5 min integrations have been used). Such averaging was chosen to achieve reasonable sensitivity for both parameters. All reconstructed light curves are presented in Figs 8 and 9. We assumed that a flare is detected when the absolute value of Stokes parameter V is above 2σ limit. In addition to the quiescent emission, we detected four short-duration events ($\Delta t \sim 3$ min), three left-circular polarization flares at epochs EG065D, EG065E and EG082E, and one right-circular polarization flare at epoch EG082E. Also we observed one broader increase of the flux in the left-circular polarization spanning ~ 10 min (EG053b). Our observations make it possible to detect flares to within 3σ sensitivity of 0.6 mJy during an averaged 3.5 min integration. The peak flux density of circularly polarized burst range from 0.5 to 2 mJy, with overall fractions of circular polarization ~ 75 per cent–100 per cent.

It is accepted that the quiescent radio emission appears due to the gyrosynchrotron radiation (e.g. Osten et al. 2006). The short duration of radio flares and high circular polarization suggest coherent process and electron cyclotron maser was proposed as its likely source (e.g. Hallinan et al. 2008). The electron cyclotron maser radiation is emitted at the electron cyclotron frequency $\nu_c \simeq 2.8 \times 10^6 B$ Hz, where B is the strength of magnetic field in the radio emission region. We conducted observations at 4.99 GHz and this frequency infers the small-scale magnetic field strength of $B \simeq 1.8$ kG. The observed flares are mostly left circularly polarized, in a good agreement with other published observations at 4.9 GHz (Hallinan et al. 2007). This supports the model proposed by these authors to explain periodic flares with period $P = 1.96$ h that reflects the rotation period of TVLM513. In this model, TVLM513 generates broad-band, coherent radio emission in the presence of kG magnetic field in a stable, large-scale configuration.

6 CONCLUSIONS

In this work, we present new radio observations of the M9 ultra-cool dwarf TVLM513, using the EVN at 4.99 GHz. These observations were conducted in the framework of our RISARD survey (Gawronski et al. 2013). TVLM513 has been detected at all seven

scheduled epochs between 2011 March and 2015 March. It proves an excellent performance and sensitivity of the EVN.

Combining earlier astrometric data from Forbrich & Berger (2009) and Forbrich et al. (2013) with our measurements, we updated the astrometric model and the annular parallax $\pi = 93.27^{+0.18}_{-0.17}$ mas. Unfortunately, the measurements sampling is sparse, and EVN data are systematically less accurate than VLBA data gathered by Forbrich et al. (2013). Therefore we could not detect any clear pattern of the residuals to the free-falling motion of the target. The irregular residuals pattern makes it possible to rule out putative companions more massive than Saturn in $\gtrsim 7$-yr orbit or Jupiter in $\gtrsim 1$-yr orbit. The astrometric positions exhibit a significant error floor ~ 0.43 mas, which is comparable with the astrometric model residuals. This may suggest that the target is either a single object, either a putative, yet unresolved Jupiter-mass range companion is present in a short-period orbit (up to one year) contributing to the apparent, residual noise. Revealing the presence of such a companion would need, however, much dense sampling of the astrometric positions and better accuracy than at present can be reached with the EVN.

Yet the accuracy of derived astrometric positions of TVLM513 is comparable with the expected *Gaia* mission outcome. Our results could be a good reference as an independent observational experiment and will make it possible to better determine the proper motion and a potential geometric curvature of the target motion.

The gathered observational data show a variability of the radio flux on long and short time-scales, consistent with published data in earlier papers (e.g. Berger et al. 2008). We detected four highly circularly polarized radio flares. The short durations of the flares and degrees of circular polarization are indicative of a coherent emission, which most likely emerges due to the electron cyclotron maser mechanism. In this context, the inferred local magnetic field is about 1.8 kG, similar to values found for other low-mass and fully convective stars (e.g. Morin et al. 2010).

REFERENCES

Affer L. et al., 2016, A&A, 593, A117
Allred J. C., Hawley S. L., Abbett W. P., Carlsson M., 2006, ApJ, 644, 484
Antonova A., Doyle J. G., Hallinan G., Bourke S., Golden A., 2008, A&A, 487, 317
Antonova A., Hallinan G., Doyle J. G., Yu S., Kuznetsov A., Metodieva Y., Golden A., Cruz K. L., 2013, A&A, 549, A131
Astudillo-Defru N. et al., 2015, A&A, 575, A119
Bailey J., Butler R. P., Tinney C. G., Jones H. R. A., O'Toole S., Carter B. D., Marcy G. W., 2009, ApJ, 690, 743
Baraffe I., Chabrier G., Barman T. S., Allard F., Hauschildt P. H., 2003, A&A, 402, 701

Benz A. O., Conway J., Gudel M., 1998, A&A, 331, 596

Berger E., 2002, ApJ, 572, 503

Berger E., 2006, ApJ, 648, 629

Berger E. et al., 2001, Nature, 410, 338

Berger E. et al., 2008, ApJ, 673, 1080

Bower G. C., Bolatto A., Ford E. B., Kalas P., 2009, ApJ, 701, 1922

Bower G. C., Bolatto A., Ford E. B., Fries A., Kalas P., Sanchez K., Sanderbeck P., Viscomi V., 2011, ApJ, 740, 32

Bowler et al., 2015, ApJ, 806, 62

Chibueze J. O. et al., 2014, PASJ, 66, 104

Forbrich J., Berger E., 2009, ApJ, 706, L205

Forbrich J., Berger E., Reid M. J., 2013, ApJ, 777, 70

Foreman-Mackey D., Hogg D. W., Lang D., Goodman J., 2013, PASP, 125, 306

Gawronski M. P., Gozdziewski K., Katarzynski K., 2013, Proc. Sci., Project RISARD. SISSA, Trieste, PoS (11th EVN Symposium)043

Goodman J., Weare J., 2010, Commun. Appl. Math. Comput. Sci., 1, 65

Güdel M., Benz A. O., 1993, ApJ, 405, L63

Hallinan G., Antonova A., Doyle J. G., Bourke S., Brisken W. F., Golden A., 2006, ApJ, 653, 690

Hallinan G. et al., 2007, ApJ, 663, L25

Hallinan G., Antonova A., Doyle J. G., Bourke S., Lane C., Golden A., 2008, ApJ, 684, 644

Hallinan G. et al., 2015, Nature, 523, 568

Kaplan G. H., Bangert J. A., Barron E. G., Bartlett J. L., Puatua W., Harris W., Barrett P., 2012, IAU Joint Discussion Vol. 7, IAU Joint Discussion, Naval Observatory Vector Astrometry Software (NOVAS) Version 3.1:Fortran, C, and Python Editions. p. P24 (Available at http://referencesystems.info/iau-joint-discussion-7.html)

Kirkpatrick J. D., Henry T. J., Irwin M. J., 1997, AJ, 113, 1421

Leto P., Trigilio C., Buemi C. S., Umana G., Ingallinera A., Cerrigone L., 2016, MNRAS, preprint (arXiv:1611.00511)

Morin J., Donati J.-F., Petit P., Delfosse X., Forveille T., Jardine M. M., 2010, MNRAS, 407, 2269

Neupert W. M., 1968, ApJ, 153, L59

Osten R. A., Hawley S. L., Allred J., Johns-Krull C. M., Brown A., Harper G. M., 2006, ApJ, 647, 1349

Pestalozzi M. R., Benz A. O., Conway J. E., Güdel M., 2000, A&A, 353, 569

Ravi V., Hallinan G., Hobbs G., Champion D. J., 2011, ApJ, 735, L2

Reid I. N., Kirkpatrick J. D., Liebert J., Gizis J. E., Dahn C. C., Monet D. G., 2002, AJ, 124, 519

Reid M. J., Menten K. M., Brunthaler A., Zheng X. W., Moscadelli L., Xu Y., 2009, ApJ, 693, 397

Reiners A., Basri G., 2007, ApJ, 656, 1121

Rivera E. J. et al., 2005, ApJ, 634, 625

Sahlmann J., Lazorenko P. F., Ségransan D., Martín E. L., Queloz D., Mayor M., Udry S., 2013, A&A, 556, A133

Sahlmann J., Lazorenko P. F., Ségransan D., Martín E. L., Mayor M., Queloz D., Udry S., 2015, A&A, 577, A15

Sahlmann J. et al., 2016, A&A, 595, A77

Tinney C. G., Reid I. N., Gizis J., Mould J. R., 1995, AJ, 110, 3014

Williams P. K. G., Casewell S. L., Stark C. R., Littlefair S. P., Helling C., Berger E., 2015, ApJ, 815, 64

Wolszczan A., Route M., 2014, ApJ, 788, 23

This paper has been typeset from a TEX/LATEX file prepared by the author.